

Article

High Performance of Mn-Doped MgAlO_x Mixed Oxides for Low Temperature NO_x Storage and Release

Chenchen Cui ¹, Junwei Ma ², Zhongpeng Wang ^{1,*} , Wei Liu ¹, Wenxu Liu ¹ and Ligu Wang ^{1,*}

¹ School of Water Conservation and Environment, University of Jinan, 336 West Road of Nanxinzhuang, Jinan 250022, China

² Environmental Protection Monitoring Station of Anqiu, Shandong Province, Middle Section of Gongnong Road, Anqiu 262100, China

* Correspondence: chm_wangzp@ujn.edu.cn (Z.W.); chm_wanglg@ujn.edu.cn (L.W.);
Tel.: +86-531-8276-9233 (Z.W.); +86-136-9861-3168 (L.W.)

Received: 19 July 2019; Accepted: 7 August 2019; Published: 9 August 2019



Abstract: NO_x storage-reduction (NSR) is a potential approach for the effective removal of NO_x under the lean conditions in lean-burn engines. Herein, manganese-doped mixed oxides (Mn/MgAlO_x) with high performance for low temperature NO_x storage and release were derived from hydrotalcites precursors prepared by a facile coprecipitation method. The catalysts were characterized by X-ray diffraction (XRD), SEM, N₂ adsorption-desorption, H₂-TPR, FT-IR, and X-ray photoelectron spectroscopy (XPS) techniques. The Mn-doped MgAlO_x catalysts exhibited high NO_x storage capacity (NSC) at low temperature range (150–300 °C), which was related to their increased surface area, improved reducibility and higher surface Mn³⁺ content. The largest NSC measured, 426 μmol/g, was observed for NO_x adsorption at 200 °C on Mn15 catalyst (the sample containing 15 wt% of Mn). The in situ DRIFTS spectra of NO_x adsorption proved that the Mn-doped hydrotalcite catalysts are preferred for low temperature NO_x storage and release due to their ability to store NO_x mainly in the form of thermally labile nitrites. NSR cycling tests revealed the NO_x removal rate of Mn15 sample can reach above 70% within the wide temperature range of 150–250 °C. Besides, the influence of CO₂, soot, H₂O and SO₂ on NO_x storage performance of Mn15 catalyst was also studied. In all, owing to their excellent NO_x storage capacity, NSR cycling performance, and resistance to CO₂, soot, SO₂ and H₂O, the Mn-doped MgAlO_x NSR catalysts have broad application prospects in NO_x control at low temperatures.

Keywords: hydrotalcite; manganese; NO_x storage; release; low temperature

1. Introduction

The Lean-burn engines (diesel and lean-burn gasoline engines) are gradually being promoted and applied due to their high fuel economy and low pollution emissions. Traditional three-way catalysts (TWC), however, have low NO_x removal efficiency under lean-burn conditions, which are not satisfied with the strict emission standards. NO_x storage and reduction (NSR) technology is a potential method to effectively solve the problem of vehicle exhaust pollution [1–3]. NSR operates in a cyclic pattern with alternating lean-burn and rich-burn periods. Under lean-burn conditions, NO is oxidized to NO₂ by the active component of the catalysts and stored in the form of nitrite or nitrate. While in the very short rich-burn conditions, stored NO_x can be released and reduced, at the same time, the catalysts are regenerated [4,5]. A typical NSR catalyst is primarily composed of active component (generally a noble metal), storage component (an alkali metal or alkaline earth metal) and supports having large specific surface area. Presently, Pt/BaO/Al₂O₃ system is regarded as a model NSR catalyst and has been extensively studied [6–9]. Nevertheless, this catalyst system also has some disadvantages, such as the

inferior resistance to SO₂, CO₂ and water vapor, as well as thermal degradation. Many strategies have been reported to solve these problems, for example, looking for the best Pt/Ba ratio [10,11], using MgO or CaO instead of BaO [12], adding various metal components [13–15], or applying hydrotalcite-like materials and their derivatives, et al. Furthermore, it is worth noting that although Pt/BaO/Al₂O₃ catalyst exhibits excellent activity at higher temperatures (> 300 °C) owing to the powerful basicity of BaO, it has insufficient NO_x storage capability at low temperatures. It is reported that the typical engine-out temperatures are about 150–350 °C [2]. Therefore, how to exploit the NSR catalysts with good low temperature activity is an urgent problem to be solved in this field.

Mn-based mixed oxides have been thoroughly studied at length and proved to exhibit good low-temperature activity for selective catalytic reduction (SCR), NO oxidation and simultaneous soot-NO_x removal. Wu et al. [16] reported MnO_x/TiO₂ mixed oxides for low-temperature NH₃-SCR. They found that the conversion rate of NO_x can reach nearly 100% at 120–220 °C after adding Ce, and doping V to MnO_x/TiO₂ catalysts can efficiently increase the selectivity of nitrogen. Tian et al. [17] prepared three different morphologies MnO₂ using a hydrothermal method and observed that MnO₂ nanorods exhibited the highest activity for reduction of NO_x with conversion efficiencies of above 90% in the range of 250–300 °C. Qi et al. [18] investigated the Mn-Ce mixed oxides for NO oxidation and found that the incorporation of ZrO₂ into MnO_x-CeO₂ can improve the NO oxidation activity. Additionally, Mn has been proved to be an effective dopant for Ba-based NO_x storage and reduction catalysts due to its higher NO oxidizability [19–21]. Li et al. [22] studied the hydrotalcite-based Mn_xMg_{3-x}AlO catalysts and revealed that the Mn⁴⁺ ions are the most active species for soot combustion and simultaneous soot-NO_x removal.

Mn-based mixed oxides also possess excellent NO_x adsorption performance at low temperatures. Guo et al. [23] investigated MnO_x catalysts with different calcination temperatures for NO adsorption and noticed that the catalyst calcined at 550 °C containing a single α-Mn₂O₃ phase exerted the best NO adsorbability. Machida et al. [24,25] observed that Mn-Ce oxides have superior NO_x removal at temperatures lower than 150 °C. Huang et al. [26] studied a sequence of Fe-Mn-based metal oxides for NO_x adsorption at 25 °C and pointed out that they were efficient catalysts for NO_x removal. Sun et al. [27] reported that Mn-Sn-Ce-O catalysts with different Sn/(Mn + Sn + Ce) molar ratios showed higher NO_x storage capacity at 100 °C, with Mn_{0.4}Sn_{0.5}Ce_{0.1} showing the highest NSC of 565.9 μmol/g. Recently, Guo et al. [28] systematically studied the NO_x storage and release in the alternative lean-burn/rich-burn atmospheres over Mn₂O₃, Mn₃O₄ and MnO₂ catalysts at low temperatures (≤ 200 °C) and found that Mn₂O₃ showed high NO oxidizability and MnO₂ had the biggest NO_x storage capacity. They suggested that the Mn³⁺ ions and surface-active oxygen species are the key to high NO oxidation activity. Zeng et al. [29] found that MnO_x-CeO₂ catalysts exhibited stronger ability to adsorb NO_x and resistance to SO₂ poisoning than that of MnO_x-TiO₂ catalysts, which was attributed that MnO_x-CeO₂ catalysts possess more Mn³⁺ and surface adsorbed oxygen.

Recently, well-dispersed metal oxides derived from hydrotalcite-like compounds (also called layered double hydroxides, LDH) have aroused wide attention from researchers due to their special layer structure, exchangeability of anions, stronger basicity, memory effect and superior thermostability [30–32], wherefore they are attractive active environmental catalysts and promising substitution of the commercial NSR catalysts. Whereas, similar to Pt/BaO/Al₂O₃ NSR catalysts, Mg/Al hydrotalcite derived oxides also have inferior performance in NO_x storage and release at low temperatures. Extensive researches have shown that the incorporation of active component (e.g., Cu [33], Fe [34], Co [35], Ag [36]) into hydrotalcite precursors can effectively enhance the redox properties and NSR catalytic properties of the oxides' catalysts.

In consideration of excellent NO oxidation activity of Mn-based oxides and potential NO_x storage performance of hydrotalcites catalysts, a series of Mn-doped MgAlO_x catalysts derived from hydrotalcites were prepared as alternative NSR catalysts and their low-temperature performance have been studied in the present work. The Mn-doped oxides were synthesized using an LDH approach using a cetyltrimethyl ammonium bromide (CTAB)-assisted co-precipitation method, which can obtain

large surface area, high metal dispersion and thermal stability. The molar ratio of divalent and trivalent metal ions in raw materials was controlled to 3:1 in order to obtain LDH precursors with high crystallinity [31]. Then we can effectively utilize the dispersing effect of LDH structure on active metal components. Specific studies were implemented to characterize the NO_x storage and release performance of samples. The surface species formed during NO_x adsorption were investigated by in situ DRIFTS measurements. Finally, the effects of CO₂, soot, H₂O and SO₂ on NO_x storage performance of Mn15 catalyst were also studied.

2. Results and Discussions

2.1. XRD Analysis

The XRD patterns of the Mn/Mg/Al hydrotalcites precursors are presented in Figure 1a. The chemical composition of the synthesized precursors, the lattice parameters, as well as mean crystallite size are displayed in Table 1. For all the precursors, the characteristic diffraction peaks at 11°, 23°, 34°, 38°, 46°, 61°, and 63° corresponding to hydrotalcite-like compound (JCPDS 22-0700) were observed, which can be assigned to the (003), (006), (009), (015), (018), (110) and (113) crystal planes, respectively. The addition of Mn to Mg/Al hydrotalcites led to the appearance of weak characteristic diffraction peaks corresponding to MnCO₃ at 2θ = 24.2°, 32°, 42.5° and 53°. Furthermore, the peak of crystal plane (003) shifted to higher 2θ angle with the increase of Mn contents, which was ascribed to lattice contraction due to the isomorphous substitution of Mg²⁺ by manganese cations with smaller ionic radius. A decrement of lattice parameter *a* was observed in Mn-based samples, implying part of Mn dopant may incorporate into the Mg/Al hydrotalcite structure. Besides, the parameter *c* decreased when dopant Mn was introduced, which was due to the revised electrostatic interactions between the layer and the interlayer network [37]. As shown in Table 1, the mean crystallite size of the Mn/Mg/Al hydrotalcite varied in the range of 9–19 nm, with the largest size of 18.8 nm for Mn10-HT sample.

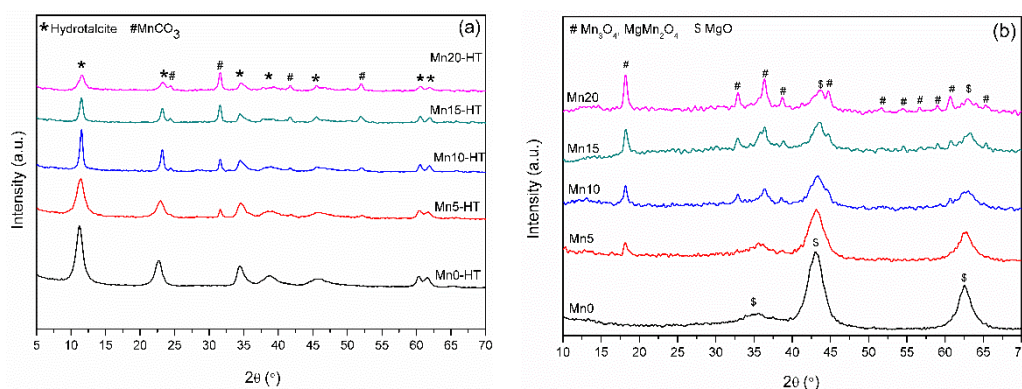


Figure 1. X-ray diffraction (XRD) patterns of hydrotalcite precursors (a) and calcined samples (b).

Table 1. Chemical compositions and lattice parameters of the synthesized hydrotalcites.

Sample	Metal Molar Ratio in Mixed Salt Solution	2θ (°) ^a	Lattice Parameter		X _s (nm) ^b
			<i>a</i> (Å)	<i>c</i> (Å)	
Mn0-HT	Mg:Al = 75:25	11.32	3.101	23.435	10.5
Mn5-HT	Mn:Mg:Al = 5:70:25	11.35	3.099	23.431	9.8
Mn10-HT	Mn:Mg:Al = 10:65:25	11.38	3.099	23.430	18.8
Mn15-HT	Mn:Mg:Al = 15:60:25	11.51	3.098	23.429	14.4
Mn20-HT	Mn:Mg:Al = 20:55:25	11.57	3.100	23.431	10.1

^a 003 crystal face. ^b Mean crystallite size calculated from the 003 and 110 crystal face according to Debye-Scherrer equation.

After calcination at 600 °C, the hydrotalcite structure was completely decomposed and new oxide derivatives were formed (Figure 1b). The diffraction patterns of Mn0 sample showed three well-defined peaks centered at 35°, 43° and 62°, which belonged to the MgO phase (JCPDS 45-0946). However, the peaks of MgO phase became gradually weaker with increasing Mn content. At the same time, new diffraction peaks at 18°, 33°, 36.5°, 38.5°, 45°, 52°, 54°, 58.5°, 60°, 61° and 65° can be observed after Mn doping, which can be attributed to Mn₃O₄ phase (JCPDS 80-0382) and/or MgMn₂O₄ spinel phase (JCPDS 23-0392). Because the peaks position of Mn₃O₄ and MgMn₂O₄ spinel are very similar, it is difficult to differentiate them from the XRD results.

2.2. SEM Analysis

The morphology of the calcined oxides catalysts was studied by SEM as demonstrated in Figure 2. After calcination at 600 °C, the hydrotalcite-like layer structure was collapsed and small particles of mixed oxides were formed. The particles were agglomerated together, which may be related to the high temperature calcination. Mn0 sample exhibited a worm-like structure with plentiful intergranular pores. No distinct morphological changes can be observed on Mn5 sample. However, Mn15 catalyst showed a spherical shape nanoclusters structure. Small pores formed by the accumulation of elementary particles were observed on all oxides, which was in favor of the gaseous reaction in the catalytic process [38].

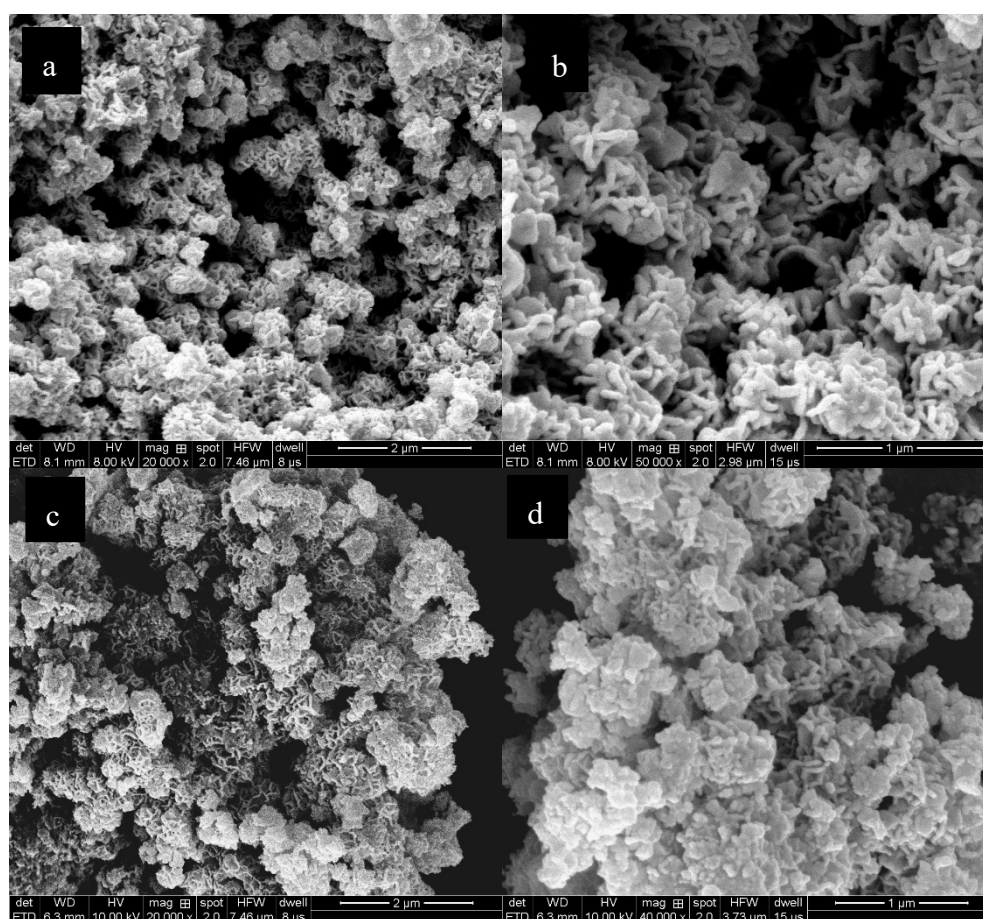


Figure 2. Cont.

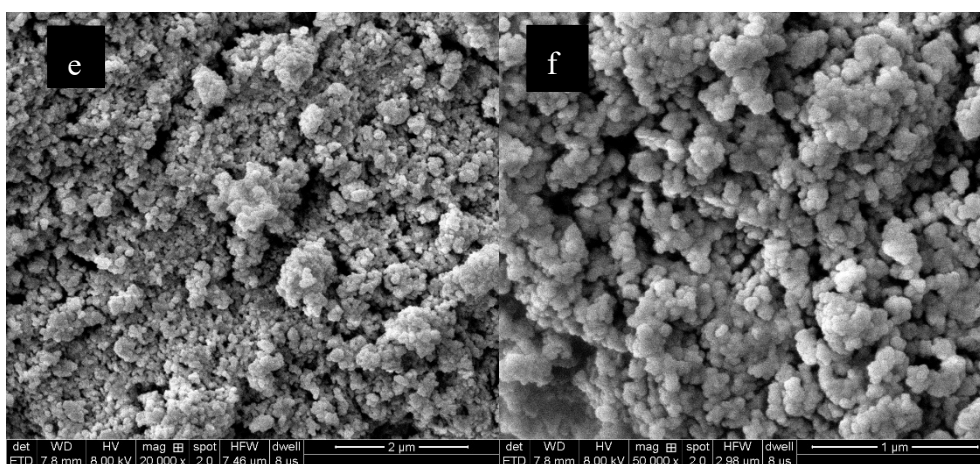


Figure 2. SEM images of Mn0 (a,b), Mn5 (c,d) and Mn15 (e,f).

2.3. N_2 Adsorption-Desorption Characterization

The nitrogen adsorption-desorption isotherms and pore size distributions of the catalysts are exhibited in Figure 3. All the hydrotalcites-derived mixed oxides showed IUPAC type IV isotherms, indicating that the hydrotalcite-like samples produced mesoporous mixed oxides after calcined at 600 °C. The H3 type of hysteresis loops indicate a capillary condensation in a high P/P_0 range of 0.6–1.0 [39]. The hysteresis loop is usually found in adsorbents containing slit-shaped pores.

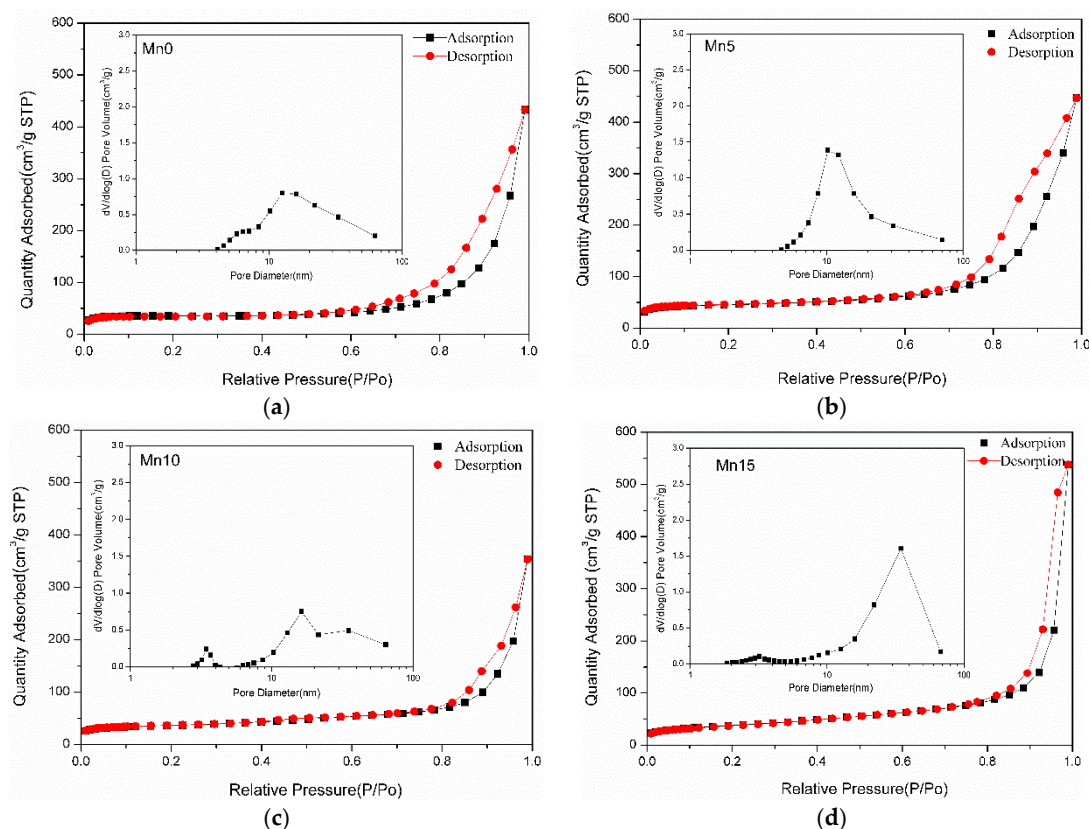


Figure 3. Cont.

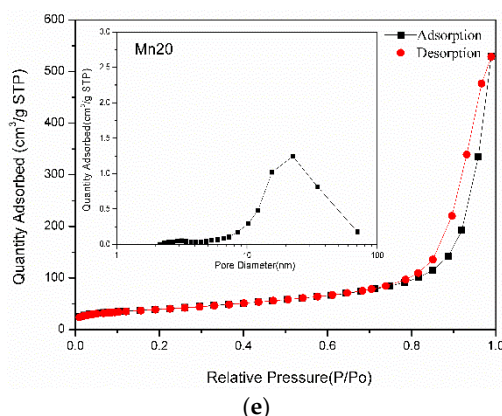


Figure 3. N₂ adsorption/desorption isotherms of Mn-doped MgAlO_x mixed oxides. (a) Mn0; (b) Mn5; (c) Mn10; (d) Mn15; (e) Mn20.

As seen from the pore size distribution curves, a large proportion of pores fell in mesopores range ($2 \text{ nm} < r_p < 50 \text{ nm}$) with a fraction in macro size, suggesting that the catalysts are hierarchical porous materials. The specific surface areas, pore volume and average pore diameter of samples are presented in Table 2. All the samples showed relatively large surface areas of $100\text{--}140 \text{ m}^2\cdot\text{g}^{-1}$. Mn substitution substantially increased the specific surface areas of the samples. The high surface areas can offer more accessible active sites for NO_x adsorption on the catalysts. The averaged pore diameter varied in the range of $14\text{--}23 \text{ nm}$, which was beneficial for gas molecule diffusion in the pores during NO_x adsorption and desorption process [32].

Table 2. Textural properties of the oxide catalysts.

Sample	SBET ^a (m ² ·g ⁻¹)	VP ^b (cm ³ ·g ⁻¹)	DP ^c (nm)
Mn0	108	0.67	16.9
Mn5	144	0.68	14.3
Mn10	136	0.55	16.0
Mn15	133	0.83	22.6
Mn20	139	0.82	19.6

^a The BET specific surface area. ^b Total pore volume. ^c Average pore diameter.

2.4. XPS and H₂-TPR Characterization

X-ray photoelectron spectroscopy (XPS) characterization was implemented on samples in order to define the surface species. The XPS spectra of Mn2p and O1s are showed in Figure 4. As shown in Figure 4a, the Mn 2p XPS spectra of the Mn5, Mn10, Mn15 and Mn20 samples presented two peaks centered at around 642.7 eV and 654.2 eV, corresponding to Mn 2p_{3/2} and Mn 2p_{1/2}, respectively [40]. The Mn 2p_{3/2} peak was relatively wide, because manganese existed in different oxidation states on the surface of the catalysts. By deconvoluting, it can be fitted into three peaks located at around 643.9 eV, 642.7 eV and 641.2 eV, corresponding to Mn⁴⁺, Mn³⁺, and Mn²⁺, respectively [41]. Additionally, surface Mn³⁺ was reported to perform better catalytic activity than Mn⁴⁺ and Mn²⁺ in the NO oxidation reaction [28,29,42]. In order to define the relative concentration of Mn³⁺ ions in samples, the molar ratio of Mn³⁺/(Mn³⁺ + Mn⁴⁺) was calculated from XPS results and summarized in Table 3. As shown, Mn15 and Mn20 samples possessed higher surface Mn³⁺ content compared to others.

O1s spectra in Figure 4b exhibit two fitted oxygen peaks, which correspond to two types of surface oxygen species. The peak centered at ~531.2 eV can be assigned to lattice oxygen (O_{latt}) [43], while the peak at ~532.6 eV can be assigned to surface adsorbed oxygen (O_{ads}) [44,45]. We calculated the value of O_{ads}/(O_{latt} + O_{ads}) to roughly estimate the amount of surface adsorbed oxygen for all samples and the obtained results are illustrated in Table 3. After addition of Mn, the surface adsorbed oxygen content

decreased. However, further increase of Mn doping had no significant effect on the surface adsorbed oxygen content. It can be speculated that the surface adsorbed oxygen content was not a decisive factor in the NO_x storage capacity.

H₂-TPR experiments were performed to study the reducibility of the catalysts. The TPR profiles are displayed in Figure 5. No reduction peak was observed on Mn0 sample. However, after Mn doping, two peaks located at about 250 °C and 460 °C appeared, which can be ascribed to the reduction of Mn₃O₄ [46]. Based on literature reports, the lower temperature peak was ascribed to the reduction of Mn⁴⁺ → Mn³⁺, whereas the higher temperature peak was ascribed to the reduction of Mn³⁺ → Mn²⁺ [18,47]. Obviously, the higher temperature reduction peak was stronger, which may also include the reduction of Mn³⁺ in MgMn₂O₄ spinel. Therefore, the H₂-TPR data was basically consistent with the phase composition of the catalysts in XRD analysis. Mn₃O₄ and MgMn₂O₄ spinel are the main crystalline phase besides brucite MgO, especially for oxides samples with higher Mn content. As shown in Table 3, relative Mn³⁺ content estimated from integrated reduction peak areas increased with increasing Mn doping. Mn15 and Mn20 samples had higher Mn³⁺ content compared to others, which was in keeping with XPS results.

Interestingly, as the Mn content increased, the first reduction peak shifted to lower temperature range, indicating that Mn doping can improve the reducibility of the samples. The H₂ consumption of all samples was calculated and the results were listed in Table 3. It can be concluded that with the increase of Mn content, more H₂ was consumed. Noticeably, Mn15 catalyst possessed the highest H₂ consumption of 34.86 mmol·g⁻¹.

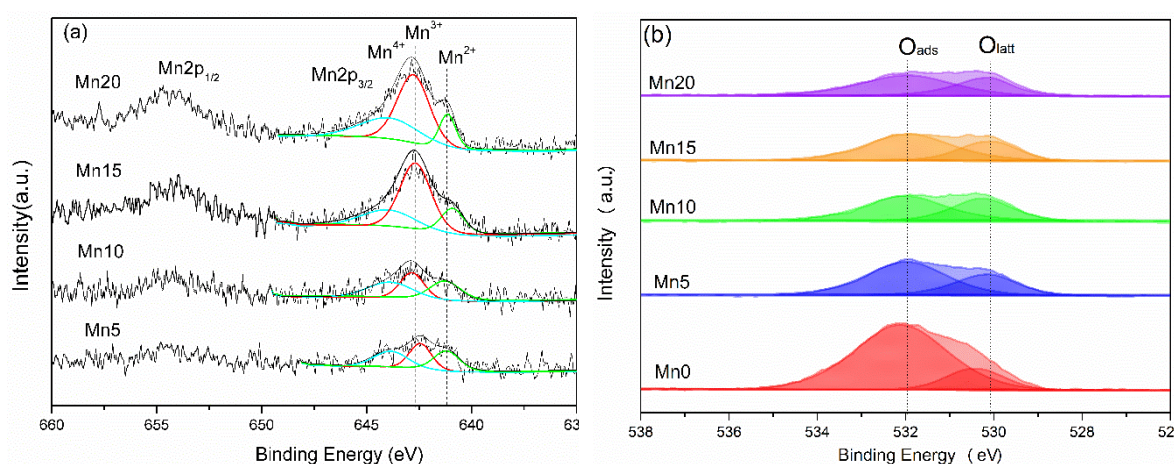


Figure 4. X-ray photoelectron spectroscopy (XPS) spectra for Mn2p (a) and O1s (b) of the catalysts.

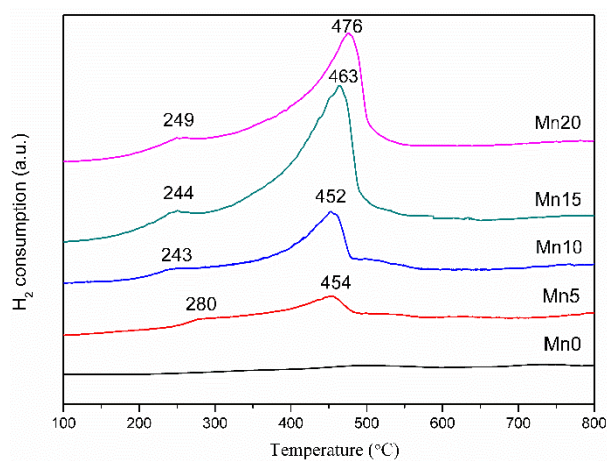


Figure 5. H₂-TPR profiles of the samples.

Table 3. X-ray photoelectron spectroscopy (XPS) and H₂-TPR results of samples.

Sample	Mn ³⁺ /(Mn ³⁺ + Mn ⁴⁺) (%)	O _{ads} /(O _{latt} + O _{ads}) (%)	H ₂ Consumption ^a (mmol·g ⁻¹)	Mn ³⁺ % ^b
Mn0	-	82	0	-
Mn5	47	65	6.51	69
Mn10	51	57	10.32	76
Mn15	67	65	34.86	82
Mn20	62	64	21.34	78

^a The total H₂ consumption of the reduction peaks from 100 to 800 °C. ^b Relative Mn³⁺ content estimated from integrated reduction peak areas.

2.5. NO_x Adsorption and Desorption Behavior

NO_x adsorption experiments were implemented at 300 °C to investigate the effect of Mn incorporation on NO_x storage. The obtained NO_x concentration profiles are showed in Figure S1. At the initial stage of adsorption, no NO_x was monitored in the outlet, indicating NO_x was all adsorbed on the catalysts surface. Subsequently, with increasing adsorption time, NO_x concentrations at the outlet increased continually and then reached to a steady state. This phenomenon suggested that the adsorption process achieved a stable equilibrium. Additionally, in the whole process, small amount of NO₂ was detected at the outlet, indicating the oxidation of NO to NO₂ on the catalysts. With the increase of Mn content, the NO₂ percentage at the outlet after adsorption saturation was 5.7%, 12.5%, 17.5%, 25.0%, 25.2%, respectively, revealing that the dopant Mn can facilitate the oxidation of NO into NO₂.

The NO_x storage efficiency (NSE) based on the NO_x adsorption profiles are summarized in Table 4. At the beginning of storage (less than 1 min), NO_x was all stored on the oxides catalysts. However, differences in NSE became increasingly obvious with increasing storage time. Mn doping resulted in higher NSE, for example, an NSE of about 60% was achieved for Mn15 and Mn20 catalysts compared with 39.5% NSE for Mn0 sample after 30 min storage. It is related to the fact that Mn was profitable for the oxidation of NO into NO₂, which was stored more effectively.

The NO_x desorption profiles of the catalysts after NO_x adsorption at 300 °C are displayed in Figure S1. For Mn0 catalyst, the NO_x desorption followed a two-step process, corresponding to the desorption of various nitrites and nitrates, respectively. NO was the primary species and less than 20 ppm NO₂ over 200–700 °C was produced. After Mn doping, the NO_x desorption followed a one-step process, and the peak temperature of desorption shifted to lower temperature, indicating that Mn decreased the stability of the formed nitrite and nitrate species. The NO_x storage capacity (NSC) of the catalysts calculated from desorption profiles are displayed in Figure 6. It is noticeable that the NSC significantly increased from 50 μmol/g for Mn0 sample to about 160–200 μmol/g after Mn doping, indicating that Mn played a key role in NO_x storage. The improvement can be ascribed to the increased surface area, promoted oxidation of NO into NO₂, and high surface adsorbed oxygen species. Notably, Mn15 sample showed the best NO_x storage capacity (206 μmol/g) at 300 °C. When the dopant Mn continued to increase, the NO_x storage capacity decreased. The decrease in Mn20 indicated that the doping amount of Mn has a threshold value, beyond which it is not conducive to storage.

In the above studies, Mn15 catalyst had superior NO_x storage performance, so we further investigated its NO_x storage performance at different adsorption temperatures (150, 200, 250, 300 and 350 °C). The experimental results are presented in Figure S2. Generally speaking, NO was completely trapped by the samples at the outset and almost no NO_x was monitored at the reactor outlet. With increasing reaction time, NO and a small amount of NO₂ gradually increased and finally reached a certain level. When the catalysts reached adsorption saturation at different temperatures, the NO₂ concentrations at the outlet were 70 ppm, 106 ppm, 145 ppm, 223 ppm, 375 ppm, and 377 ppm, respectively. This reflected that NO oxidation took place on catalysts during NO_x adsorption, and higher adsorption temperatures were profitable to promote the conversion of NO to NO₂. The NO_x storage efficiency (NSE) of Mn15 sample at different temperatures are summarized in Table 5. NSE of 100%

was achieved on all the samples for less than 1 min. Nevertheless, NSE value decreased with increasing reaction time. Within 10 min, over 50% NSE was found on NO_x adsorption at 150–350 °C, indicating that Mn15 catalyst can effectively store NO_x at low temperature ranges.

Figure S2 shows the desorption progress of NO_x on Mn15 catalyst. Apparently, NO_x desorption followed a two-step process at the adsorption temperature of 150 °C and 200 °C, corresponding to various types of nitrites and nitrates. However, after the adsorption temperature was raised, the NO_x desorption followed a one-step process. Simultaneously, NO was the main desorption species, accompanied by different amounts of NO₂ depending on the adsorption temperature. The NSC calculated from the desorption profiles of Mn15 sample at different temperatures are listed in Figure 7. Mn15 catalyst possessed better NO_x storage capacity of above 200 μmol/g in the temperature range of 150–300 °C. The highest NSC was observed at 200 °C of 426 μmol/g on Mn15. Nevertheless, when the adsorption temperature continued to increase, the NO_x storage capacity decreased. This decrement was probably due to the decomposition of stored nitrite and nitrate by thermodynamic instability. At the same time, we compared other types of oxide catalysts with excellent NO_x storage activity reported in recent years. The NO_x storage performance of different types of catalysts is summarized in the Table S1. It can be seen that the Mn15 catalyst can still exhibit high NO_x storage capacity at low temperatures compared to the bimetallic oxides and La-containing perovskite-type oxide catalysts, even higher than the costly storage of precious metal Pt-based catalysts and the conventional Pt/BaO/Al₂O₃ catalysts.

Table 4. NO_x storage efficiency of the catalysts at 300 °C.

Time (min)	NO _x Storage Efficiency (%)				
	Mn0	Mn5	Mn10	Mn15	Mn20
1	100	100	100	100	100
5	62.8	69.2	79.9	87.2	91.3
10	39.5	46.4	55.1	60.7	63.4
30	18.9	23.1	26.0	28.4	28.9
60	12.9	16.1	17.3	19.2	19.4

Table 5. NO_x storage efficiency of Mn15 sample at different temperatures.

Time (min)	NO _x Storage Efficiency (%)				
	150 °C	200 °C	250 °C	300 °C	350 °C
1	100	100	100	100	100
5	96.1	88.3	80.5	87.2	93.4
10	69.1	57.5	52.3	60.7	64.2
30	32.5	24.2	24.3	28.4	30.3
60	22.9	14.2	15.0	19.2	21.3

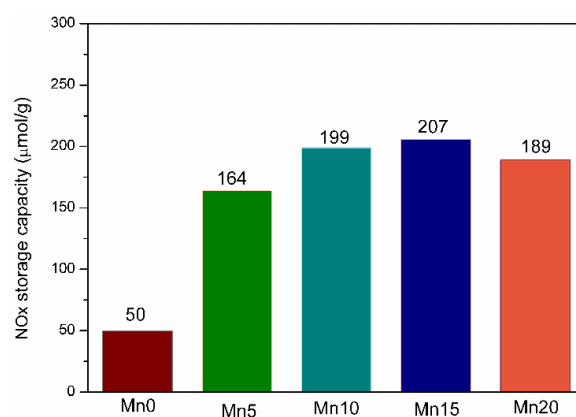


Figure 6. NO_x storage capacity of the catalysts at 300 °C.

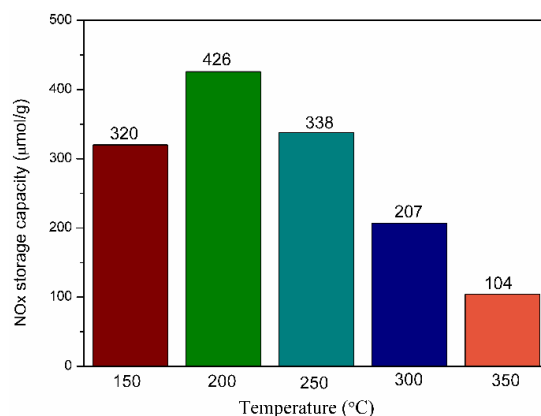


Figure 7. NO_x storage capacity of Mn15 sample at different temperatures.

2.6. In Situ DRIFTS Spectra

The in situ DRIFTS spectra experiments were carried out at 300 °C on Mn0, Mn5 and Mn15 catalysts to probe the adsorbed species formed during NO_x storage. Generally, they were various nitrites and nitrates. The specific species are summarized in Table 6. As can be seen from Figure 8a, when NO + O₂ was introduced to Mn0 catalyst, the peak at 1230 cm⁻¹ attributed to bridged bidentate nitrite appeared within 1 min and its intensity increased with increasing adsorption time. The weak peak located at 1310 cm⁻¹ belonged to bridged bidentate nitrate appeared after 5 min. This indicated nitrites were the dominant adsorbed species on Mn0 sample. For Mn5 catalyst, nitrites were formed rapidly in the initial period. Subsequently, the intensity of nitrates increased whilst that of nitrites decreased, indicating that NO adsorbed on Mn5 to form nitrites and then formed NO₂ and stable nitrates [48–50]. In other words, the storage of NO on Mn5 catalyst followed the “nitrite” pathway. Similar formation and conversion were observed on Mn15 sample. The bands at 1312 cm⁻¹ and 1447 cm⁻¹ due to monodentate nitrate were the primary NO_x species stored on Mn15 catalyst. Compared with Mn5 sample, the rate of nitrite transformation on Mn15 catalyst was higher than that on Mn5 catalyst, revealing that Mn content played a favorable role in the oxidation of nitrite.

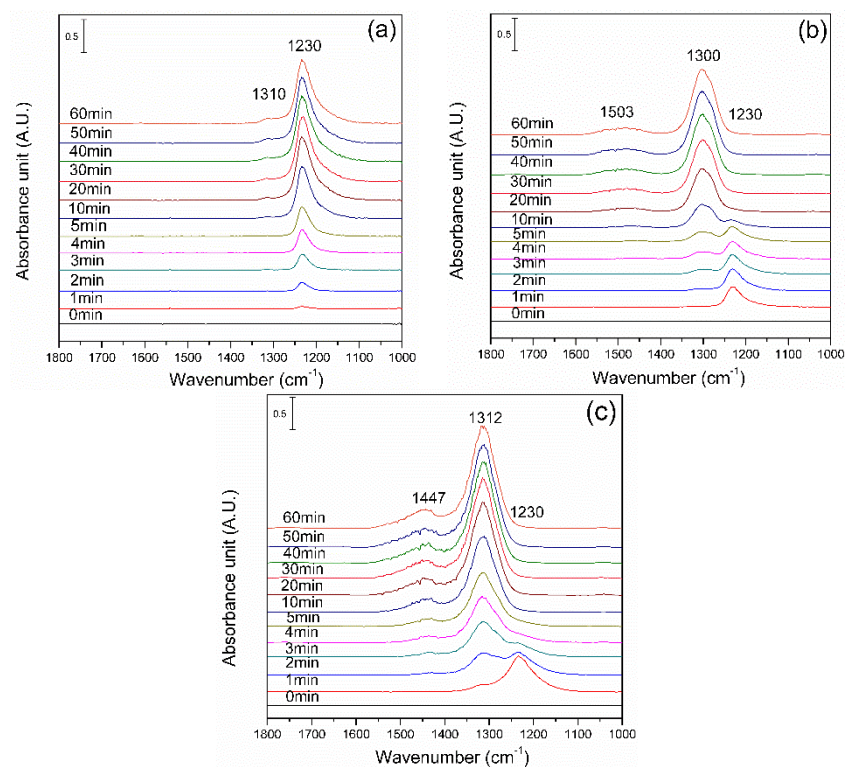
Figure 9 shows the in situ DRIFTS spectra of Mn15 sample after exposure to NO + O₂ at different temperatures for 60 min. The specific species are summarized in Table 7. At 150 °C, the broad peak located at 1220 cm⁻¹ was assigned to bridged bidentate nitrite, corresponding to the adsorption of NO on the weak basic sites [32,51]. The weak peak at 1321 cm⁻¹ was associated with bridged bidentate nitrate. For adsorption at 200 °C, the peaks at 1226 cm⁻¹ assigned to bridged bidentate nitrite appeared in the initial stage and later shifted to 1310 cm⁻¹ and 1480 cm⁻¹ that ascribed to bridged bidentate nitrate and monodentate nitrate, indicating a conversion from nitrite to nitrate on the sample. The species formed at 250 °C and 300 °C were similar to that at 200 °C. Differently, the rate of nitrite oxidation was improved with increasing adsorption temperature, indicating high adsorption temperatures accelerated the transformation of nitrites to nitrates. Besides, the peak intensity of nitrate species increased, suggesting high temperatures were favorable to form more stable nitrates species. For adsorption at 350 °C, only bridged bidentate nitrate (1315 cm⁻¹) and monodentate nitrate (1438 cm⁻¹) were formed and became the major species in the final period, implying the storage of NO on the sample followed the “nitrate” pathway. Besides, their intensities increased with an increment in adsorption time. It is concluded that, within 10 min of adsorption, the NO_x adsorbed species on Mn15 catalyst were mainly various nitrites at lower temperatures (<300 °C), while NO_x was mainly stored in the form of nitrate at higher temperatures (≥300 °C). Therefore, Mn-doped hydrotalcite catalysts are preferred for low temperature NO_x storage and release may because they can store NO_x as thermally labile nitrites.

Table 6. Characteristic vibrations of adsorbed NO_x species on Mn0, Mn5, Mn15 catalysts.

NO _x Species	Structure	IR Bands/cm ⁻¹		
		Mn0	Mn5	Mn15
Bridged bidentate nitrite		1230	1226	
Bridged bidentate nitrate		1310	1310 1480	
Monodentate nitrate				1312 1447
Chelating bidentate nitrate			1503	

Table 7. Characteristic vibrations of adsorbed NO_x species on Mn15 catalyst.

NO _x Species	Structure	IR Bands/cm ⁻¹				
		150 °C	200 °C	250 °C	300 °C	350 °C
Bridged bidentate nitrite		1220	1230	1237	1237	
Bridged bidentate nitrate		1321	1300	1312	1312	1315
Monodentate nitrate				1445	1445	1438
Chelating bidentate nitrate			1503			

**Figure 8.** In situ DRIFTS spectra of NO_x adsorption at 300 °C on Mn0 (a), Mn5 (b) and Mn15 (c).

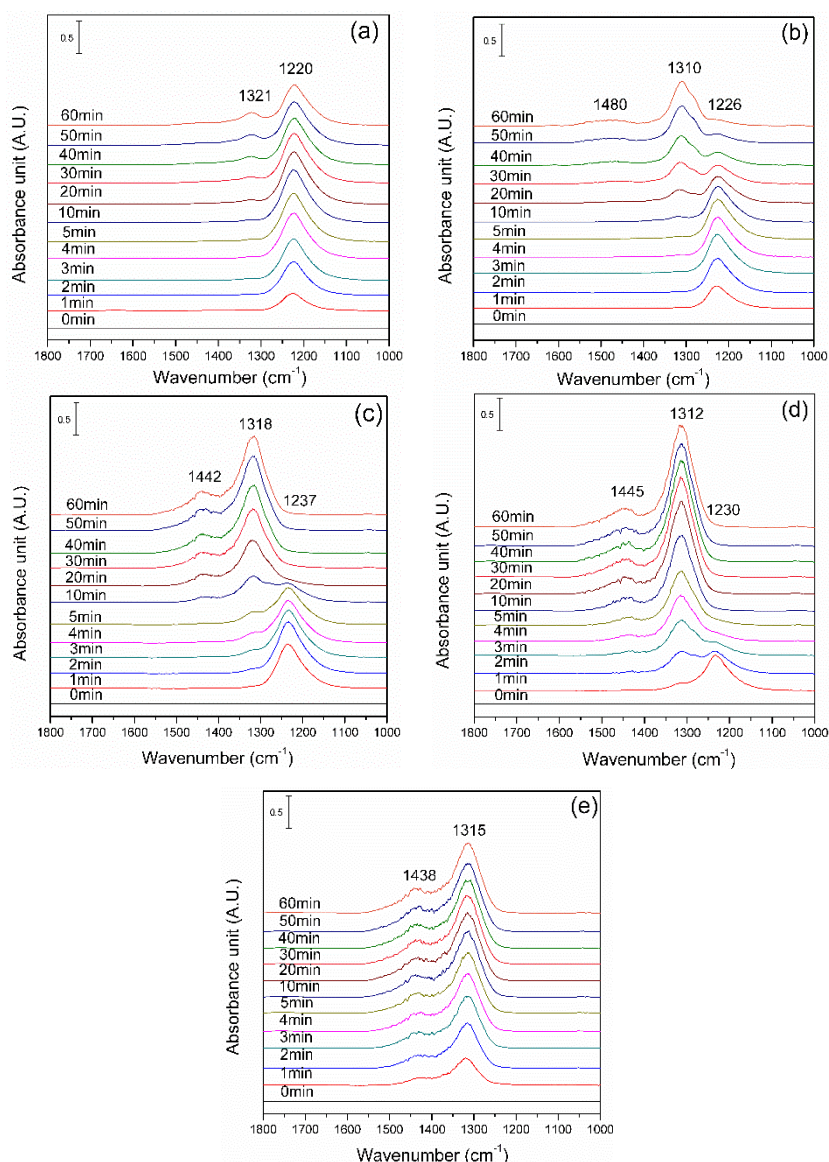


Figure 9. In situ DRIFTS spectra of NO_x adsorption on Mn15 sample at 150 °C (a), 200 °C (b), 250 °C (c), 300 °C (d), 350 °C (e).

2.7. NO_x Lean-Rich Cycling Performance

The lean-rich cycling experiments were also tested on Mn15 sample at different temperatures and the results are displayed in Figure S3. During the lean periods, NO was first oxidized to NO_2 and then NO_2 was stored in the form of nitrate or nitrite. During rich periods, the stored thermodynamic instability nitrite and nitrate were decomposed and release NO_x . Subsequently, the released NO_x was reduced by H_2 . As shown in Figure 10, it can be found that the average removal rate of the Mn15 sample can reach above 70% in the range of 150–250 °C. Nevertheless, with increasing reaction temperature, the average removal rate decreased, indicating that Mn15 sample had better lean-rich cycling performance at lower temperatures than that at higher temperatures. It was in accordance with the isothermal NO_x adsorption and desorption results. This may be related to the fact that NO_x was mainly stored in the form of labile nitrite at lower temperatures, while NO_x was mainly stored in the form of stable nitrate at higher temperatures. It has been known that nitrites were more easily decomposed than nitrates, which was profitable to the regeneration of the catalysts, thus improving the average removal rate of the catalysts.

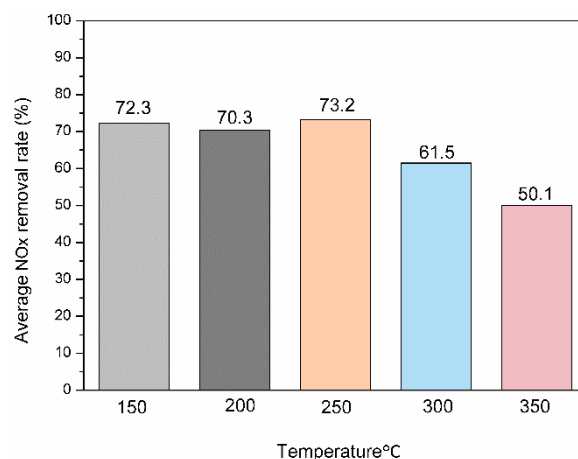


Figure 10. Average NO_x removal rate of Mn15 sample at different temperatures during lean-rich cycling experiments.

2.8. The Influence of CO₂, Soot, H₂O, and SO₂

To further investigate the influence of CO₂, soot, H₂O and SO₂ on catalysts, the isothermal NO_x storage performance tests were carried out on Mn15 sample at 200 °C. As shown in Figure 11, after the introduction of CO₂, soot, H₂O and SO₂, the NO_x storage performance of Mn15 catalyst had different degrees of decrement. Or rather, after adding CO₂, the NO_x storage capacity of the sample slightly decreased from 426 μmol/g to 409 μmol/g, which was attributed that CO₂ competed with NO_x for chemical adsorption sites [52]. Similar results were observed on soot-catalyst mixtures. It may be related to the fact that the exothermic combustion of soot destabilized the stored species and the soot combustion produced CO₂ would compete with NO_x for storage sites on the catalyst.

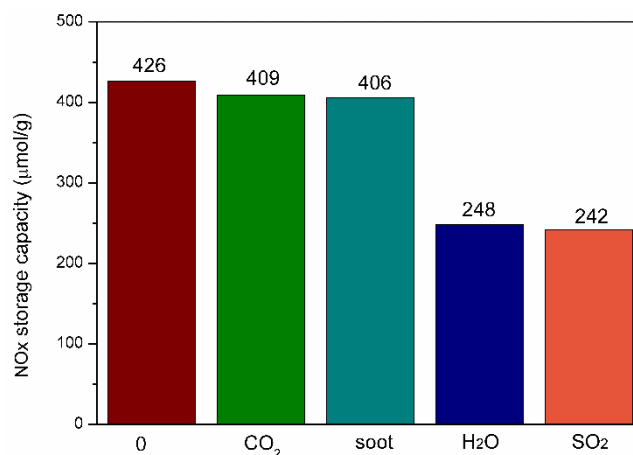


Figure 11. The influence of CO₂, soot, H₂O and SO₂ on the NO_x storage capacity at 200 °C.

According to reports [53], the total exhaust usually contains about 2–15% H₂O, thus the influence of water vapor on the NO_x storage was examined. It can be clearly seen that H₂O restrained the NO_x storage capacity by close to 42%, which was due to the competitive adsorption between NO_x and H₂O on the surface of the catalyst [54]. Then SO₂ was also taken into consideration, the NSC significantly decreased from 426 μmol/g to 242 μmol/g. This deactivation caused by SO₂ could be related to the formation of sulfites and sulfates, which would decrease the basicity of the storage sites. In conclusion, during the NO_x storage and release process, Mn15 catalyst exhibited high resistance to CO₂ and soot, with a certain sulfur and water resistance.

3. Experimental

3.1. Preparation of Catalysts

The Mn/Mg/Al hydrotalcites precursors were prepared using a cetyltrimethyl ammonium bromide (CTAB)-assisted co-precipitation method [55]. The mixed salt solution is composed of metal nitrates of $\text{Mg}(\text{NO}_3)_2 \cdot 6\text{H}_2\text{O}$, $\text{Al}(\text{NO}_3)_3 \cdot 9\text{H}_2\text{O}$ and $\text{Mn}(\text{NO}_3)_2 \cdot 4\text{H}_2\text{O}$ with disparate metal molar ratio displayed in Table 1. The mixed basic solution includes 2 M NaOH and 1 M Na_2CO_3 . The two solutions were simultaneously added dropwise into deionized water at constant pH = 10.0 under mechanical stirring. Then, the CTAB (with a 0.1:1 ratio of CTAB to metal ions) solution was added into the mixed solution. The achieved precipitate was suspended and stirred at 60 °C for 18 h. After filtration, it was thoroughly washed with anhydrous ethanol and deionized water until the pH of the filtrate was around 7. The filtered precipitates were dried at 80 °C for 12 h to receive hydrotalcites precursors. In the end, the as-prepared hydrotalcites were calcined at 600 °C in air for 6 h to obtain the mixed oxide catalysts, marked as Mn0, Mn5, Mn10, Mn15 and Mn20, respectively.

3.2. Catalysts Characterization

The X-ray diffraction (XRD) patterns were measured on a BRUKER-AXS D8Adance X-ray Diffractometer (Bruker, Berlin, Germany) operating at 40 kV and 30 mA using Cu K α radiation ($\lambda = 1.5418 \text{ \AA}$). The scanning angle (2θ) range was 5–90° with a step size of 0.02° and the scanning speed was 6°/min.

The scanning electron microscopy (SEM) images were observed on a Quanta FEG250 instrument (FEI, Houston, TX, USA) with an accelerating voltage of 10 kV. Prior to each test, catalysts were sprayed with gold for better conductivity.

N_2 adsorption/desorption experiments were conducted on a Micromeritics ASAP 2460 surface area analyzer (Micromeritics Instruments, Norcross, GA, USA). The samples were outgassed at 300 °C under vacuum for 6 h before analysis. The specific surface areas of the catalysts were determined according to the BET equation. The desorption curves of the catalyst were analyzed by BJH (Barrett-Joyner-Halenda) method to obtain the mean pore size and pore size distribution.

X-ray photoelectron spectroscopy (XPS) analysis was performed using a Thermo Scientific Escalab 250Xi X-ray photoelectron spectrometer (Thermo Fisher Scientific, Waltham, MA, USA) equipped with Al K α X-ray radiation source. The measured binding energies were adjusted using C1s peak (BE = 284.6 eV) as standard.

H_2 temperature-programmed reduction (H_2 -TPR) measurements were conducted on a quartz reactor. The H_2 signal was detected by a thermal conductivity detector (TCD). A 50 mg catalyst (40–80 mesh) was preprocessed at 500 °C for 30 min in a flow of N_2 (50 mL/min) and then cooled to room temperature. In the end, the reactor was heated in a flow of 5% H_2/N_2 (50 mL/min) at a rate of 10 °C/min from room temperature to 900 °C. CuO was used as a calibration reference to quantify H_2 consumption.

3.3. NO_x Storage and Desorption Measurements

The isothermal NO_x storage experiments were implemented in a quartz flow reactor using 50 mg of the catalysts (40–80 mesh). Samples were pretreated at 500 °C for 1 h in N_2 and then cooled to the experimental temperature. When the temperature stabilized at the experimental temperature, the flow gas of 1000 ppm NO + 5 vol.% O_2 in He at a rate of 100 mL/min was introduced for 1 h for NO_x adsorption. Concentrations of NO, NO_2 and NO_x from the reactor outlet was detected by the chemiluminescence NO_x analyzer (Model 42i-HL, Thermo Fisher Scientific, Waltham, MA, USA.).

The NO_x storage efficiency (NSE) was calculated by integrating the concentration curves of NO_x according to the following Equation (1).

$$NSE = \left(1 - \frac{\int_0^t NO_{x,out} dt}{\int_0^t NO_{x,in} dt} \right) \times 100\% \quad (1)$$

NO_{x,in} is the NO_x concentration at the reactor inlet (ppm), NO_{x,out} is the NO_x concentration at the reactor outlet (ppm), *t* is the storage time (s).

After the NO_x adsorption, 100 mL/min N₂ was introduced to purge the catalysts for 30 min until NO_x was not detected. The temperature programmed desorption (TPD) reactions were implemented by heating the catalysts from 100 °C to 700 °C at a heating rate of 10 °C/min in 100 mL/min N₂. Concentrations of NO, NO₂ and NO_x at the reactor outlet were detected. In order to study the influence of CO₂, H₂O and SO₂ on NO_x storage, 1200 ppm CO₂, 5% water vapor or 50 ppm SO₂ were introduced to the input gases. Besides, the influence of soot was also studied. The model soot used in the present study was Printex-U provided by Degussa company. Its average particle size is 25 nm and the specific surface area is 93.5 m²/g. Elemental analysis showed that its carbonaceous nature was 90.43 wt% C, 1.09 wt% H, 0.17 wt% N and 0.51 wt% S. The volatile matter was detected to be about 5 wt% and desorbed at about 200 °C (by thermogravimetric analysis). The soot-catalyst mixture was mixed in a 1/20 weight ratio and grinded for "loose contact" condition. The NO_x storage capacity (NSC) of the catalyst was estimated by integrating the concentration curves of desorbed NO_x according to the following Equation (2).

$$NSC = \frac{\left(\int_0^t NO_{x,out} dt \right) \times F}{22.4 \times R_T \times m} \quad (2)$$

NO_{x,in} is the NO_x concentration at the reactor inlet (ppm), NO_{x,out} is the NO_x concentration at the reactor outlet (ppm), *t* is the desorption time (s). *F* is the total flow rate of the inlet gas (mL/min; STP = 0 °C, 1 atm), *R_T* is the heating rate (°C/min), *m* is the amount of the catalyst (g).

The lean-rich cycling performance of samples were investigated using a quartz flow reactor under cycling lean (120 s, 500 ppm NO and 7.5 vol.% O₂ in He) and rich (60 s, 7.5 vol.% H₂ in N₂) conditions. The overall flow rate of gas was 50 mL/min. The catalyst (50 mg) was pretreated with N₂ at 500 °C for 1 h before the tests. The NO_x removal performance was monitored as above for about 15 cycles.

3.4. In Situ DRIFTS Experiments

The in situ DRIFTS experiments of NO_x storage were conducted on a Thermal Nicolet iS50 spectrometer (Thermo Fisher Scientific, Waltham, MA, USA) equipped with a high sensitivity of MCT detector and a temperature-controllable diffuse reflection chamber. The catalysts were pretreated at 500 °C in a flow of N₂ (100 mL/min) for 30 min so as to eliminate weakly adsorbed species and then cooled to 100 °C. Simultaneously, the spectra of the catalysts in the flow of N₂ served as the background was recorded. After the pretreatment, 1000 ppm NO and 5 vol.% O₂ in He was introduced at the experimental temperature (the overall flow rate = 100 mL/min), and then the chronological DRIFTS spectra were recorded.

4. Conclusions

The performance of Mn-doped hydrotalcites derived oxides (Mn/MgAlO_x) were investigated for low temperature NO_x storage and reduction in this paper. The incorporation of Mn into hydrotalcites changed the crystal phases, structural, redox and surface properties of the oxide catalysts, with Mn₃O₄ and MgMn₂O₄ spinel as the main crystalline phase besides brucite MgO. Mn doping resulted in an evident increment in catalysts surface area and pore size, and the redox behavior was also improved. The XPS results indicated that Mn15 and Mn20 catalysts possessed more Mn³⁺, which played a favorable role in NO oxidation. Mn doped MgAlO_x catalysts exhibited high NO_x storage capacity at

low temperatures (150–300 °C). It is related to its greater surface area, improved reducibility and higher surface Mn³⁺ content. The largest NSC measured, 426 μmol/g, was observed for NO_x adsorption at 200 °C on the sample containing 15 wt% of Mn (Mn15). NO_x was stored in the form of nitrites on oxides at lower temperature (<300 °C), while nitrates at higher temperatures. The Mn-doped oxides catalysts are preferred for low temperature NO_x storage and release due to its ability to store NO_x as thermally labile nitrites. During the lean-rich cycling tests, the average NO_x removal rate can reach above 70% after Mn doping. Mn15 catalyst displayed high resistance to CO₂ and soot, with a certain sulfur and water resistance. In short, these Mn-doped hydrotalcite catalysts exhibit excellent performance in low temperatures NO_x storage and release and can be used as alternative NSR catalysts.

Supplementary Materials: The following are available online at <http://www.mdpi.com/2073-4344/9/8/677/s1>, Figure S1: NO_x adsorption and desorption profiles of the samples: (a)Mn0, (b)Mn5, (c)Mn10, (d) Mn15, (e) Mn20 catalysts at 300 °C. (Reaction conditions: 1000 ppm NO, 5 vol.% O₂, balanced with He, 100 mL/min; STP = 0 °C, 1 atm), Figure S2: NO_x adsorption and desorption profiles of Mn15 catalyst at different temperatures (a)150 °C, (b)200 °C, (c)250 °C, (d)300 °C, (e)350 °C (Reaction conditions: 1000 ppm NO, 5 vol.% O₂, balanced with He, 100 mL/min; STP = 0 °C, 1 atm), Figure S3: lean- rich cycling performance of Mn15 sample at different temperatures (a)150 °C, (b)200 °C, (c)250 °C, (d)300 °C, (e)350 °C (lean condition: 500 ppm NO, 7.5 vol.% O₂, balanced with He, 50 mL/min; rich condition: 5 vol.% H₂, balanced with N₂, 50 mL/min; STP = 0 °C, 1 atm), Table S1: Summary of catalysts NO_x storage capacity and reaction conditions.

Author Contributions: Conceptualization, C.C. and Z.W.; methodology, J.M. and W.L. (Wei Liu); software, W.L. (Wenxu Liu); validation, Z.W., J.M. and L.W.; formal analysis, C.C., J.M. and W.L. (Wei Liu); investigation, C.C.; resources, L.W.; data curation, C.C.; writing—original draft preparation, C.C.; writing—review and editing, Z.W.; visualization, C.C.; supervision, Z.W. and L.W.; project administration, Z.W.; funding acquisition, Z.W. and L.W.

Funding: This research was funded by the National Natural Science Foundation of China (No. 21777055), Shandong Provincial Natural Science Foundation (No.ZR2017BB004), Shandong Province Key Research and Development Plan (No. 2017GGX202004, 2019GSF109116), and Shandong Province Major Science and Technology Innovation Project (No. 2017CXGC1004). The APC was funded by the National Natural Science Foundation of China (No. 21777055).

Conflicts of Interest: The authors declare no conflict of interest.

References

1. Wang, P.; Yi, J.; Gu, W.; Luo, P.; Lei, L. The influence of xMn_yCe/γ-Al₂O₃ on NO_x catalysts on the properties of NO_x storage and reduction over Pt-Ce-Ba/γ-Al₂O₃ catalysts. *Chem. Eng. J.* **2017**, *325*, 700–707. [CrossRef]
2. Zhang, Z.; Shi, C.; Bai, Z.; Li, M.; Chen, B.; Crocker, M. Low temperature H₂-plasma assisted NO_x storage and reduction over the combined Pt/Ba/Al and LaMnFe catalyst. *Catal. Sci. Technol.* **2017**, *7*, 145–158. [CrossRef]
3. Ting, A.W.-L.; Harold, M.P.; Balakotaiah, V. Elucidating the mechanism of fast cycling NO_x storage and reduction using C₃H₆ and H₂ as reductants. *Chem. Eng. Sci.* **2018**, *189*, 413–421. [CrossRef]
4. Yang, R.; Cui, Y.; Yan, Q.; Zhang, C.; Qiu, L.; O'Hare, D.; Wang, Q. Design of highly efficient NO_x storage-reduction catalysts from layered double hydroxides for NO_x emission control from naphtha cracker flue gases. *Chem. Eng. J.* **2017**, *326*, 656–666. [CrossRef]
5. Bai, Z.F.; Chen, B.B.; Yu, L.M.; Zhao, Q.; Crocker, M.; Shi, C. The function of Pt in plasma-assisted NO_x storage and reduction. *Catal. Commun.* **2017**, *102*, 81–84. [CrossRef]
6. Szailer, T.; Kwak, J.H.; Kim, D.H.; Hanson, J.C.; Peden, C.H.F.; Szanyi, J. Reduction of stored NO_x on Pt/Al₂O₃ and Pt/BaO/Al₂O₃ catalysts with H₂ and CO. *J. Catal.* **2015**, *239*, 51–64. [CrossRef]
7. Su, Y.; Kabin, K.S.; Harold, M.P.; Amiridis, M.D. Reactor and in situ FTIR studies of Pt/BaO/Al₂O₃ and Pd/BaO/Al₂O₃ NO_x storage and reduction (NSR) catalysts. *Appl. Catal. B Environ.* **2007**, *71*, 207–215. [CrossRef]
8. Kumar, A.; Harold, M.P.; Balakotaiah, V. Isotopic studies of NO_x storage and reduction on Pt/BaO/Al₂O₃ catalyst using temporal analysis of products. *J. Catal.* **2010**, *270*, 214–223. [CrossRef]
9. Mulla, S.; Chaugule, S.; Yezerets, A.; Currier, N.; Delgass, W.; Ribeiro, F.; Ribeiro, F. Regeneration mechanism of Pt/BaO/Al₂O₃ lean NO_x trap catalyst with H₂. *Catal. Today* **2008**, *136*, 136–145. [CrossRef]
10. Amberntsson, A.; Fridell, E.; Skoglundh, M. Influence of platinum and rhodium composition on the NO_x storage and sulphur tolerance of a barium based NO_x storage catalyst. *Appl. Catal. B Environ.* **2003**, *46*, 429–439. [CrossRef]

11. Piacentini, M.; Strobel, R.; Maciejewski, M.; Pratsinis, S.; Baiker, A. Flame-made Pt–Ba/Al₂O₃ catalysts: Structural properties and behavior in lean-NO_x storage-reduction. *J. Catal.* **2006**, *243*, 43–56. [[CrossRef](#)]
12. Basile, F.; Fornasari, G.; Grimandi, A.; Livini, M.; Vaccari, A. Effect of Mg, Ca and Ba on the Pt-catalyst for NO_x storage reduction. *Appl. Catal. B Environ.* **2006**, *69*, 58–64. [[CrossRef](#)]
13. Iizuka, H.; Kaneeda, M.; Shinotsuka, N.; Kuroda, O.; Higashiyama, K.; Miyamoto, A. Improvement in heat resistance of NO_x trap catalyst using Ti–Na binary metal oxide as NO_x trap material. *Appl. Catal. B Environ.* **2010**, *95*, 320–326. [[CrossRef](#)]
14. Takahashi, N.; Suda, A.; Hachisuka, I.; Sugiura, M.; Sobukawa, H.; Shinjoh, H. Sulfur durability of NO_x storage and reduction catalyst with supports of TiO₂, ZrO₂ and ZrO₂–TiO₂ mixed oxides. *Appl. Catal. B Environ.* **2007**, *72*, 187–195. [[CrossRef](#)]
15. Park, S.M.; Park, J.W.; Ha, H.-P.; Han, H.-S.; Seo, G. Storage of NO₂ on potassium oxide co-loaded with barium oxide for NO_x storage and reduction (NSR) catalysts. *J. Mol. Catal. A Chem.* **2007**, *273*, 64–72. [[CrossRef](#)]
16. Wu, X.; Si, Z.; Li, G.; Weng, D.; Ma, Z. Effects of cerium and vanadium on the activity and selectivity of MnO_x–TiO₂ catalyst for low-temperature NH₃–SCR. *J. Rare Earths* **2011**, *29*, 64–68. [[CrossRef](#)]
17. Tian, W.; Yang, H.; Fan, X.; Zhang, X. Catalytic reduction of NO_x with NH₃ over different-shaped MnO₂ at low temperature. *J. Hazard. Mater.* **2011**, *188*, 105–109. [[CrossRef](#)] [[PubMed](#)]
18. Qi, G.; Li, W. NO oxidation to NO₂ over manganese-cerium mixed oxides. *Catal. Today* **2015**, *258*, 205–213. [[CrossRef](#)]
19. Zhang, Z.S.; Chen, B.B.; Wang, X.K.; Xu, L.; Au, C.; Shi, C.; Crocker, M. NO_x storage and reduction properties of model manganese-based lean NO_x trap catalysts. *Appl. Catal. B Environ.* **2015**, *165*, 232–244. [[CrossRef](#)]
20. Le Phuc, N.; Courtois, X.; Can, F.; Royer, S.; Marecot, P.; Duprez, D. NO_x removal efficiency and ammonia selectivity during the NO_x storage-reduction process over Pt/BaO(Fe, Mn, Ce)/Al₂O₃ model catalysts. Part II: Influence of Ce and Mn–Ce addition. *Appl. Catal. B Environ.* **2011**, *102*, 362–371. [[CrossRef](#)]
21. Xiao, J.H.; Li, X.H.; Deng, S.F.; Wang, R.; Wang, L.F. NO_x storage-reduction over combined catalyst Mn/Ba/Al₂O₃–Pt/Ba/Al₂O₃. *Catal. Commun.* **2008**, *9*, 563–567. [[CrossRef](#)]
22. Li, Q.; Meng, M.; Xian, H.; Tsubaki, N.; Li, X.; Xie, Y.; Hu, T.; Zhang, J. Hydrotalcite-Derived Mn_xMg_{3–x}AlO Catalysts Used for Soot Combustion, NO_x Storage and Simultaneous Soot–NO_x Removal. *Environ. Sci. Technol.* **2010**, *44*, 4747–4752. [[CrossRef](#)] [[PubMed](#)]
23. Guo, L.; Xian, H.; Li, Q.-F.; Chen, D.; Tan, Y.-S.; Zhang, J.; Zheng, L.-R.; Li, X.-G. NO adsorption behaviors of the MnO_x catalysts in lean-burn atmospheres. *J. Hazard. Mater.* **2013**, *260*, 543–551. [[CrossRef](#)] [[PubMed](#)]
24. Machida, M.; Uto, M.; Kurogi, D.; Kijima, T. MnO_x–CeO₂ binary oxides for catalytic NO_x sorption at low temperatures. Sorptive removal of NO_x. *Chem. Mater.* **2000**, *12*, 3158–3164. [[CrossRef](#)]
25. Machida, M. NO_x-Sorbent Metal Oxides, MnO_x–CeO₂. Oxidative NO Adsorption and NO_x–H₂ Reaction. *Catal. Surv. Jpn.* **2002**, *5*, 91–102. [[CrossRef](#)]
26. Huang, H.Y.; Yang, R.T. Removal of NO by Reversible Adsorption on Fe–Mn Based Transition Metal Oxides. *Langmuir* **2001**, *17*, 4997–5003. [[CrossRef](#)]
27. Sun, X.X.; Qu, R.Y.; Lei, Y.; Bai, B.Y.; Chang, H.Z.; Peng, Y.; Su, W.K.; Zhang, C.Z.; Li, J.H. Lean NO_x–SnO₂–CeO₂ catalyst at low temperatures. *Catal. Today* **2015**, *258*, 556–563. [[CrossRef](#)]
28. Guo, L.H.; Guo, L.D.; Zhao, Y.Z.; Gao, N.; Tian, Y.; Ding, T.; Zhang, J.; Zheng, L.R.; Li, X.G. Oxidizing, trapping and releasing NO_x over model manganese oxides in alternative lean-burn/fuel-rich atmospheres at low temperatures. *Catal. Today* **2017**, *297*, 27–35. [[CrossRef](#)]
29. Zeng, X.; Huo, X.; Zhu, T.; Hong, X.; Sun, Y. Catalytic Oxidation of NO over MnO_x–CeO₂ and MnO_x–TiO₂ Catalysts. *Molecules* **2016**, *21*, 1491. [[CrossRef](#)]
30. Jabłońska, M.; Palomares, A.E.; Chmielarz, L. NO_x storage/reduction catalysts based on Mg/Zn/Al/Fe hydrotalcite-like materials. *Chem. Eng. J.* **2013**, *231*, 273–280. [[CrossRef](#)]
31. Yu, J.J.; Cheng, J.; Ma, C.Y.; Wang, H.L.; Li, L.D.; Hao, Z.P.; Xu, Z.P. NO_x decomposition, storage and reduction over novel mixed oxide catalysts derived from hydrotalcite-like compounds. *J. Colloid Interface Sci.* **2009**, *333*, 423–430. [[CrossRef](#)] [[PubMed](#)]
32. Yu, J.J.; Jiang, Z.; Zhu, L.; Hao, Z.P.; Xu, Z.P. Adsorption/Desorption studies of NO_x on well-mixed oxides derived from Co–Mg/Al hydrotalcite-like compounds. *J. Phys. Chem. B* **2006**, *110*, 4291–4300. [[CrossRef](#)] [[PubMed](#)]

33. Centi, G.; Arena, G.E.; Perathoner, S. Nanostructured catalysts for NO_x storage–reduction and N₂O decomposition. *J. Catal.* **2003**, *216*, 443–454. [[CrossRef](#)]
34. Luo, J.-Y.; Meng, M.; Zha, Y.-Q.; Xie, Y.-N.; Hu, T.-D.; Zhang, J.; Liu, T. A comparative study of Pt/Ba/Al₂O₃ and Pt/Fe-Ba/Al₂O₃ NSR catalysts: New insights into the interaction of Pt–Ba and the function of Fe. *Appl. Catal. B Environ.* **2008**, *78*, 38–52. [[CrossRef](#)]
35. Vijay, R.; Hendershot, R.J.; Rivera-Jiménez, S.M.; Rogers, W.B.; Feist, B.J.; Snively, C.M.; Lauterbach, J.; Rogers, W. Noble metal free NO_x storage catalysts using cobalt discovered via high-throughput experimentation. *Catal. Commun.* **2005**, *6*, 167–171. [[CrossRef](#)]
36. Wang, T.Y.; Lu, Z.; Yang, S.H.; Sun, K. Ag/Mg-Al-O composite for low temperature NO_x storage. *Chem. Res. Chin. Univ.* **2011**, *27*, 734–738.
37. Velu, S.; Shah, N.; Jyothi, T.; Sivasanker, S. Effect of manganese substitution on the physicochemical properties and catalytic toluene oxidation activities of Mg–Al layered double hydroxides. *Microporous Mesoporous Mater.* **1999**, *33*, 61–75. [[CrossRef](#)]
38. Ai, L.; Wang, Z.; Cui, C.; Liu, W.; Wang, L. Catalytic Oxidation of Soot on a Novel Active Ca-Co Dually-Doped Lanthanum Tin Pyrochlore Oxide. *Materials* **2018**, *11*, 653. [[CrossRef](#)]
39. Zhu, H.; Xu, J.; Yichuan, Y.; Wang, Z.; Gao, Y.; Liu, W.; Yin, H. Catalytic oxidation of soot on mesoporous ceria-based mixed oxides with cetyltrimethyl ammonium bromide (CTAB)-assisted synthesis. *J. Colloid Interface Sci.* **2017**, *508*, 1–13. [[CrossRef](#)]
40. Zhang, Y.; Qin, Z.; Wang, G.; Zhu, H.; Dong, M.; Li, S.; Wu, Z.; Li, Z.; Wu, Z.; Zhang, J.; et al. Catalytic performance of MnO_x–NiO composite oxide in lean methane combustion at low temperature. *Appl. Catal. B Environ.* **2013**, *129*, 172–181. [[CrossRef](#)]
41. Zhang, P.; Lu, H.; Zhou, Y.; Zhang, L.; Wu, Z.; Yang, S.; Shi, H.; Zhu, Q.; Chen, Y.; Dai, S. Mesoporous MnCeO_x solid solutions for low temperature and selective oxidation of hydrocarbons. *Nat. Commun.* **2015**, *6*, 8446. [[CrossRef](#)] [[PubMed](#)]
42. Wu, Z.; Tang, N.; Xiao, L.; Liu, Y.; Wang, H. MnO_x/TiO₂ composite nanoxides synthesized by deposition-precipitation method as a superior catalyst for NO oxidation. *J. Colloid Interface Sci.* **2010**, *352*, 143–148. [[CrossRef](#)] [[PubMed](#)]
43. Ponce, S.; Peña, M.A.; Fierro, J. Surface properties and catalytic performance in methane combustion of Sr-substituted lanthanum manganites. *Appl. Catal. B Environ.* **2000**, *24*, 193–205. [[CrossRef](#)]
44. Dai, F.; Yu, Y.; Meng, M.; Zhang, J.; Zheng, L.; Hu, T. Effects of Synthesis Routes on the States and Catalytic Performance of Manganese Oxides Used for Diesel Soot Combustion. *Catal. Lett.* **2014**, *144*, 1210–1218. [[CrossRef](#)]
45. Larachi, F.; Pierre, J.; Adnot, A.; Bernis, A. Ce 3d XPS study of composite CexMn1–xO₂–y wet oxidation catalysts. *Appl. Surf. Sci.* **2002**, *195*, 236–250. [[CrossRef](#)]
46. Wagloehner, S.; Nitzer-Noski, M.; Kureti, S. Oxidation of soot on manganese oxide catalysts. *Chem. Eng. J.* **2015**, *259*, 492–504. [[CrossRef](#)]
47. Ji, F.; Men, Y.; Wang, J.; Sun, Y.; Wang, Z.; Zhao, B.; Tao, X.; Xu, G. Promoting diesel soot combustion efficiency by tailoring the shapes and crystal facets of nanoscale Mn₃O₄. *Appl. Catal. B Environ.* **2019**, *242*, 227–237. [[CrossRef](#)]
48. Li, L.; Shen, Q.; Cheng, J.; Hao, Z. Catalytic oxidation of NO over TiO₂ supported platinum clusters. II: Mechanism study by in situ FTIR spectra. *Catal. Today* **2010**, *158*, 361–369. [[CrossRef](#)]
49. Su, Y.; Amiridis, M.D. In situ FTIR studies of the mechanism of NO_x storage and reduction on Pt/Ba/Al₂O₃ catalysts. *Catal. Today* **2004**, *96*, 31–41. [[CrossRef](#)]
50. Nova, I. NO_x adsorption study over Pt–Ba/alumina catalysts: FT-IR and pulse experiments. *J. Catal.* **2004**, *222*, 377–388. [[CrossRef](#)]
51. Lu, P.; Zhang, X.; Wang, Z.; Tang, Q.; Wang, L.; Zhang, Z. Hydrotalcites-Derived Well-Dispersed Mixed Oxides for NO_x Adsorption and Desorption. *Sci. Adv. Mater.* **2016**, *8*, 1656–1667. [[CrossRef](#)]
52. Alcalde-Santiago, V.; Davó-Quiñonero, A.; Such-Basáñez, I.; Lozano-Castelló, D.; Bueno-López, A. Macroporous carrier-free Sr-Ti catalyst for NO_x storage and reduction. *Appl. Catal. B Environ.* **2018**, *220*, 524–532. [[CrossRef](#)]
53. Wang, X.Y.; Qi, X.X.; Chen, Z.L.; Jiang, L.L.; Wang, R.H.; Wei, K.M. Studies on SO₂ tolerance and regeneration over perovskite-type LaCo_{1–x}Pt_xO₃ in NO_x storage and reduction. *J. Phys. Chem. C* **2014**, *118*, 13743–13751. [[CrossRef](#)]

54. Wang, H.; Li, X.; Chen, M.; Zheng, X. The effect of water vapor on NO_x storage and reduction in combination with plasma. *Catal. Today* **2013**, *211*, 66–71. [[CrossRef](#)]
55. Wu, S.; Zhang, L.; Wang, X.; Zou, W.; Cao, Y.; Sun, J.; Tang, C.; Gao, F.; Deng, Y.; Dong, L. Synthesis, characterization and catalytic performance of FeMnTiO_x mixed oxides catalyst prepared by a CTAB-assisted process for mid-low temperature NH₃-SCR. *Appl. Catal. A Gen.* **2015**, *505*, 235–242. [[CrossRef](#)]



© 2019 by the authors. Licensee MDPI, Basel, Switzerland. This article is an open access article distributed under the terms and conditions of the Creative Commons Attribution (CC BY) license (<http://creativecommons.org/licenses/by/4.0/>).